OPTICA

In situ high-harmonic microscopy of a nanostructured solid

Aleksey Korobenko,[1] Sabaa Rashid,[2] Andrei Yu. Naumov,[1] David M. Villeneuve,[1] David A. Reis,[3] Pierre Berini,[2,4,5] Paul B. Corkum,[1] and Giulio Vampa[1,*]

[1]Joint Attosecond Science Laboratory, National Research Council of Canada and University of Ottawa, Ottawa, Ontario K1A 0R6, Canada
[2]Center for Research in Photonics, University of Ottawa, Ottawa, Ontario K1N 6N5, Canada
[3]Stanford PULSE Institute, SLAC National Accelerator Laboratory, Menlo Park, California, 94025, USA
[4]School of Electrical Engineering and Computer Science, University of Ottawa, Ottawa, Ontario K1N 6N5, Canada
[5]Department of Physics, University of Ottawa, Ottawa, Ontario K1N 6N5, Canada
*gvampa@uottawa.ca

Received 24 February 2023; revised 26 April 2023; accepted 8 May 2023; published 19 May 2023

Nanostructured optical surfaces allow exquisite control over linear and nonlinear light interactions, where the surface actively creates new frequencies up to high-order harmonics of an intense infrared driving laser field. The function and performance of these surfaces depend sensitively on the distribution of the high-harmonic fields in and between the nanostructured elements, as the high-harmonic wavelength becomes comparable to the nanoscale features of the surface. Imaging the nonlinear response at the active surface with nanometer resolution would greatly benefit the optimization of the metasurface's function. Here we demonstrate an approach to lensless imaging of extreme ultraviolet high harmonics that resolves the amplitude and phase of nonlinear polarization at the active nanostructured surface of an MgO crystal. Imaging the near-field distribution of high harmonics is the gateway to optimized functional high-harmonic metasurfaces and the integration of high harmonics on a chip.

https://doi.org/10.1364/OPTICA.488545

1. INTRODUCTION

Modern technology enables the reliable patterning of features on surfaces with dimensions as small as approximately 10 nm. The flip side of nanoscale fabrication is nanoscale imaging of the fabricated nanostructures and of their function. Extreme ultraviolet (XUV) light is ideally suited for imaging nanostructures because a short wavelength (shorter than ∼100 nm) confers to XUV light the required spatial resolution. In fact, the synergy between nanostructured surfaces and XUV light goes beyond imaging. Recently, dielectric nanostructures have been employed for the controlled generation of coherent XUV light [1,2], turning passive surfaces into active XUV optical components through a high-harmonic generation (HHG) process. These demonstrations of XUV metasurfaces extend the reach of previous high-harmonic work with nanostructures, which operated at visible and UV wavelengths [3–10]. Our goal in this paper is to image the nonlinear polarization that results in the emission of XUV radiation, at the nanostructured surface, to verify that the nanostructured surface controls the emission process in the desired way.

The most broadly adopted method for imaging XUV light is *lensless* imaging, whereby diffracted light scattered from the surface onto a detector is analyzed to recover both the amplitude and phase of XUV radiation at the sample. Because XUV light is absorbed by all materials, standard lens-based microscopy, such as confocal microscopy, cannot be used. Lensless imaging can be performed with holography [11–15] or with coherent diffractive imaging (CDI) [16–18], including a variation thereof known as ptychography [19]. All these implementations are able to retrieve the linear (scattering) response of a surface at visible [20], XUV [21–23] and x-ray [24–26] wavelengths. In particular, high-harmonic XUV sources, incorporating a dedicated (usually gaseous) medium and refocused on the target under study, were recently adopted for lensless imaging. They were shown to provide polarization [27], chemical [28], and magnetic [29] contrast at the nanoscale.

Existing implementations of diffractive imaging, however, are difficult or impossible to apply to imaging an active nonlinear surface for the following reasons. Holography requires a known reference source with sufficient brightness and suitable size to interfere with the scattered waves from the object. Generating a reference beam is not straightforward, since this beam has to be either produced by the active surface (and therefore not known *a priori*) or added from a secondary source and suitably overlapped with the unknown field on the detector. CDI and ptychography, instead, require oversampling of the image to recover N complex values of the electromagnetic field from N real-valued image pixels. The traditional CDI method achieves oversampling by imposing a finite-sized illumination of the object, which makes it difficult to implement with standard Gaussian beams, whereas ptychography achieves oversampling by acquiring diffraction images at several

different overlapping positions of the sample relative to the illuminating beam. Ptychography relies on the linearity of the scattering process, or at least its precisely known mathematical expression [30]. Some success was observed in applying HHG ptychography in the visible [31], assuming a simple linear scattering relationship. However, the relation of the reconstructed harmonic field to the real one remains questionable under this assumption because of the strong and non-perturbative nonlinear HHG process.

Ours is an *in situ* approach to CDI microscopy that is aptly suited to image the electric field distribution of active optical nanostructured surfaces. As illustrated in Fig. 1(a), we illuminate the nanostructured dielectric, MgO, with an infrared laser and capture the emitted high harmonics on a spatially resolved XUV detector. We opt for imaging an aperiodic structure (Fig. 2) because it is much harder to retrieve with CDI methods than periodic patterns, which result in regularly spaced, bright, Bragg spots on the detector [2]. Oversampling is achieved by scanning an absorbing mask (a fused silica membrane) in close proximity of the MgO surface, in a plane parallel to it, and recording diffraction images for various mask positions. At every position, the mask blocks only a part of the XUV beam. The resulting set of binary amplitude modulations allows us to reconstruct the XUV field at the mask position, and therefore at the MgO surface upon a simple back-propagation step. Our method is uniquely applicable to nonlinear high-harmonic metasurfaces, because oversampling is achieved without altering the nonlinear emission at the nanostructured surface, as would happen in a ptycographic approach, and it works with smooth Gaussian laser beams, avoiding the requirement of finite-sized illumination of traditional CDI. Moreover, it does not need a reference beam, as in holography. We are able to retrieve the XUV electric field distribution, both amplitude and phase, as it is generated at the nanostructured MgO surface, with a 10%–90% resolution of ≈ 183 , nm, close to the diffraction limit of the detector. We find that the XUV field is in agreement with the numerical simulations, reproducing the phase steps and amplitude oscillations near the sharp features of the structures, arising from the laser restructuring near them. Additionally, our method allows us to measure smooth variations of the phase due to self-focusing of the laser and the dipole phase of the HHG.

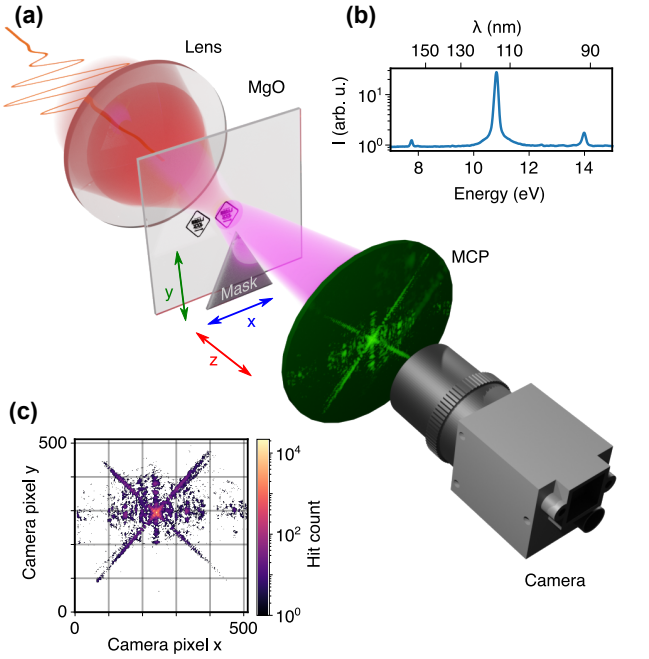

Fig. 1. Experimental setup. (a) Horizontally polarized laser pulses (red beam) are focused with a lens through the MgO sample, which is kept in a vacuum chamber (see Appendix A for the laser parameters). The MgO surface structured with nanoscale diamond-shaped logos faces the detector. The emitted XUV radiation is collected on a double microchannel plate (MCP) detector and phosphor screen. The phosphor screen is imaged from outside the chamber with a fast CMOS camera (FLIR Blackfly). The amplitude mask, a thin triangular glass membrane, is mounted on an XYZ nanopositioner (2 nm encoder resolution) and moved partially into the emitted beam path thereby changing the far-field diffracted pattern. (b) The detected high-harmonic spectrum is dominated by the seventh harmonic (114 nm wavelength). (c) Example of an acquired diffraction image. Strong diagonal stripes at 45° are due to the diffraction from the diamond-shaped contour of the illuminated structure.

2. RESULTS

Using helium-ion beam lithography [1] we fabricate a binary height profile onto a surface of the MgO crystal. The etch depth, measured with atomic-force microscopy, is $h = 60$ nm, resulting in an estimated phase difference of

$$\Delta\varphi = 2\pi h(n_{\mathrm{MgO}}(800\ \mathrm{nm}) - 1)/\lambda_{\mathrm{XUV}} \sim 2.4\ \mathrm{rad} \qquad (1)$$

between the seventh harmonic ($\lambda_{\mathrm{XUV}} = 114$ nm) emitted from the etched and pristine parts of the sample. In the above expression, $n_{\mathrm{MgO}}(800\mathrm{nm})$ is the refractive index of MgO at the laser wavelength. The emitted radiation originates from the ∼10 nm thick layer of the crystal near the interface, limited by the XUV absorption.

Illuminating the sample with the infrared laser beam, we collect a set of far-field diffraction images of the XUV harmonics, at 41 different mask positions, each image containing $\sim 5 \times 10^5$ detected photon hits. While higher-energy harmonics ($\gtrsim 25$ eV) have been observed in MgO crystals before [32,33], the long pulse duration limits the detected XUV to a single seventh harmonic of 800 nm laser at 10.8 eV [Fig. 1(b)]. One of the diffraction images is shown in Fig. 1(c). We use a fused silica membrane after the MgO crystal as the absorbing mask. Fused silica completely absorbs the seventh harmonic of the 800 nm laser and does not contribute to emission of the same harmonic. Each image is then transformed to k-space, using the calibration technique described in Appendix A. The resulting images correspond to the intensity profiles of a 2D Fourier transform of the field in the plane of the mask. Amplitude and phase of the XUV beam in this plane are reconstructed after 2000 iterations of a custom GPU-run algorithm (a few minutes of runtime) based on alternating projections approach [16]. The result in shown in Fig. 2(a), right panel. We then use a plane-wave expansion to propagate it back to the plane of the sample. To determine the sample position precisely, we carry out this propagation in 0.5 μm steps. XUV images at some of these planes are shown in Fig. 2(a). The image with the clearest pattern represents the XUV field at the sample plane.

The final result of this procedure is presented in Fig. 2(c), where the phase of the field is plotted next to the He^+ beam microscope image of the same pattern [Fig. 2(b)]. The reconstructed image nicely reproduces the features of the original pattern, including text, down to sub-micrometer scale. The smallest text remains unresolved.

To carry out a quantitative comparison, in Fig. 3, we plot lineouts of the reconstructed field phase across several sharp steps in the

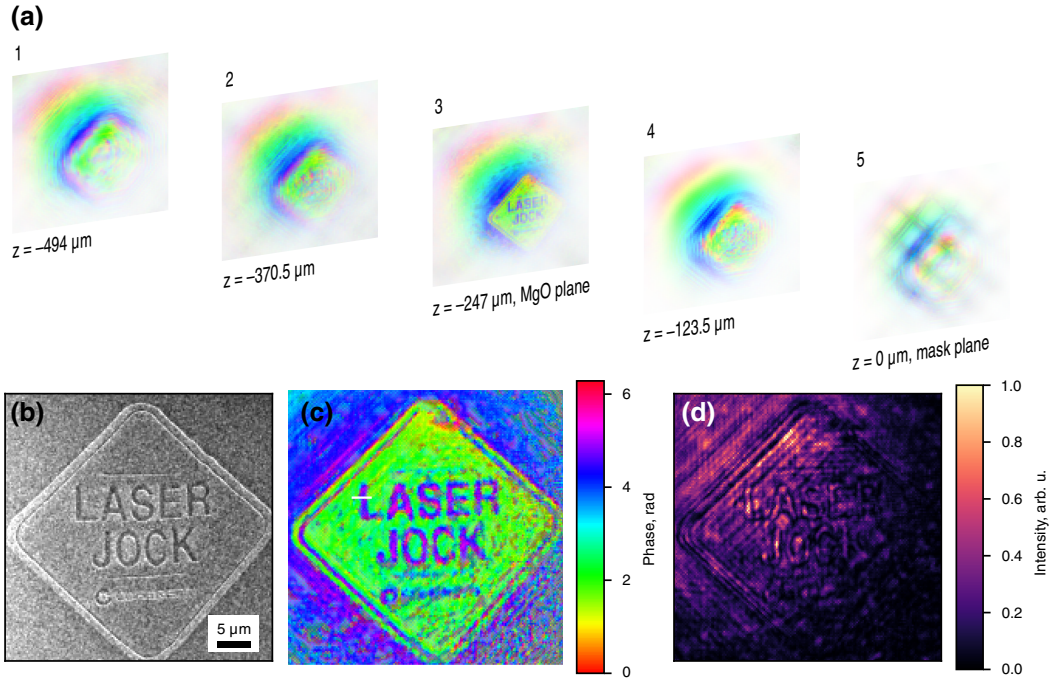

Fig. 2. Reconstruction results. (a) The reconstructed XUV field at the mask (panel 5) is numerically backpropagated to parallel planes (panels 1–4). Color represents the phase of the field, and opacity represents its intensity. At $z = 247$ µm plane (panel 3), the logo is sharpest. A constant phase term of $ik_{\mathrm{XUV}}z$, where $k_{\mathrm{XUV}} = 5.5 \times 10^5 \mathrm{cm}^{-1}$ is the wavenumber of the XUV radiation, is subtracted from every profile, to simplify their comparison. (b) Structure image acquired with a helium ion beam microscope. Reconstructed (c) phase and (d) intensity of the XUV field at the sample plane [middle figure in (a)].

letters of the "Laser jock" text (colored square symbols), aligning them horizontally for best overlap. The average of these lineouts (black curve) yields a phase step of 2.4 rad, in excellent agreement with the one predicted by Eq. (1), and a 10%–90% width of $w_{10-90} = 183$ nm, as highlighted by the red-shaded region. We simulate the 2.4 rad phase step, imaged by an optical system of numerical aperture (NA) $\mathrm{NA} = \sin\tan^{-1}\frac{D_{\mathrm{MCP}}}{2L_{\mathrm{MCP}}} = 0.2$, corresponding to the maximum transverse momentum acquired in our diffraction setup. Here, D_{MCP} is the diameter of the microchannel plate (MCP) detector, and L_{MCP} is the distance between its center and the sample. The result, highlighted as the blue-shaded region in Fig. 3, reproduces the averaged reconstructed trace well, with the 10%–90% width of 171 nm.

Since the ratio between the etch depth and the laser wavelength is $h/\lambda = 60\ \mathrm{nm}/470\ \mathrm{nm} = 0.127$, it can be assumed that the simple phase-only modulation model is inaccurate, and the laser field undergoes substantial diffraction inside the structure, leading to its restructuring. This restructuring leads to amplitude modulations of the harmonic beam, as seen in Fig. 2(d). Figure 4 presents the phase and amplitude images obtained with a more accurate modeling of the interaction. We perform 3D calculations, splitting the laser and the XUV propagation in two separate steps. The details of our method can be found in Appendix A. The phase and intensity of the calculated XUV are plotted in Figs. 4(b) and 4(e) next to the reconstruction results. The reconstructed and calculated phases, Figs. 4(a) and 4(b), agree nicely, demonstrating what is essentially a two-value function that follows the height of the structure. Interestingly, the reconstructed phase reveals a gradual decrease towards the periphery of the beam, corresponding to a converging wavefront. This is due to two competing effects: self-focusing of the high-intensity laser inside MgO, and the intensity-dependent dipole phase of the HHG process [34], with the former effect

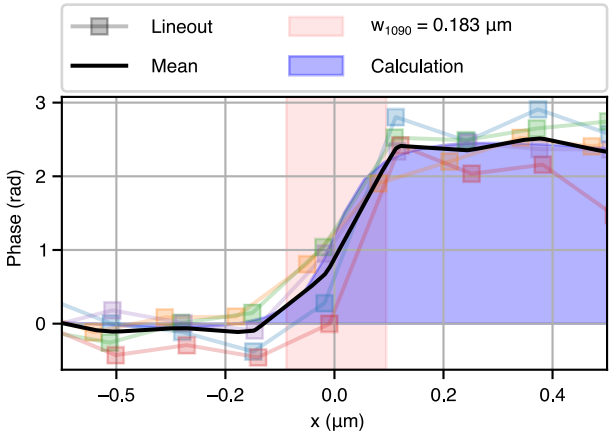

Fig. 3. Reconstructed phase lineouts (square symbols), taken along several sections near phase steps, and their average (black curve). The red shading represents the 10%–90% width of the step, 0.183 µm, and the blue shading is a simulated resolution-limited phase image of a hard 60 nm-deep step. The 10%–90% width of the latter is 170 nm, and is determined by the diffraction limit of the detector.

dominating for the crystal thickness we use. Neither of these effects is present in our calculation model, resulting in a flat phase profile in Fig. 4(b).

Similarities between the reconstruction and calculation can also be observed for the intensity profiles [Figs. 4(d) and 4(e)]. Both profiles are rather smooth, except in the vicinity of the etched steps, where some oscillations can be observed, with the intensity reaching minima at the exact step positions. However, the calculation predicts sharper field spikes around these steps. A better agreement is achieved after taking into account the finite NA of our imaging system. Limiting the spatial frequencies of the calculated profiles

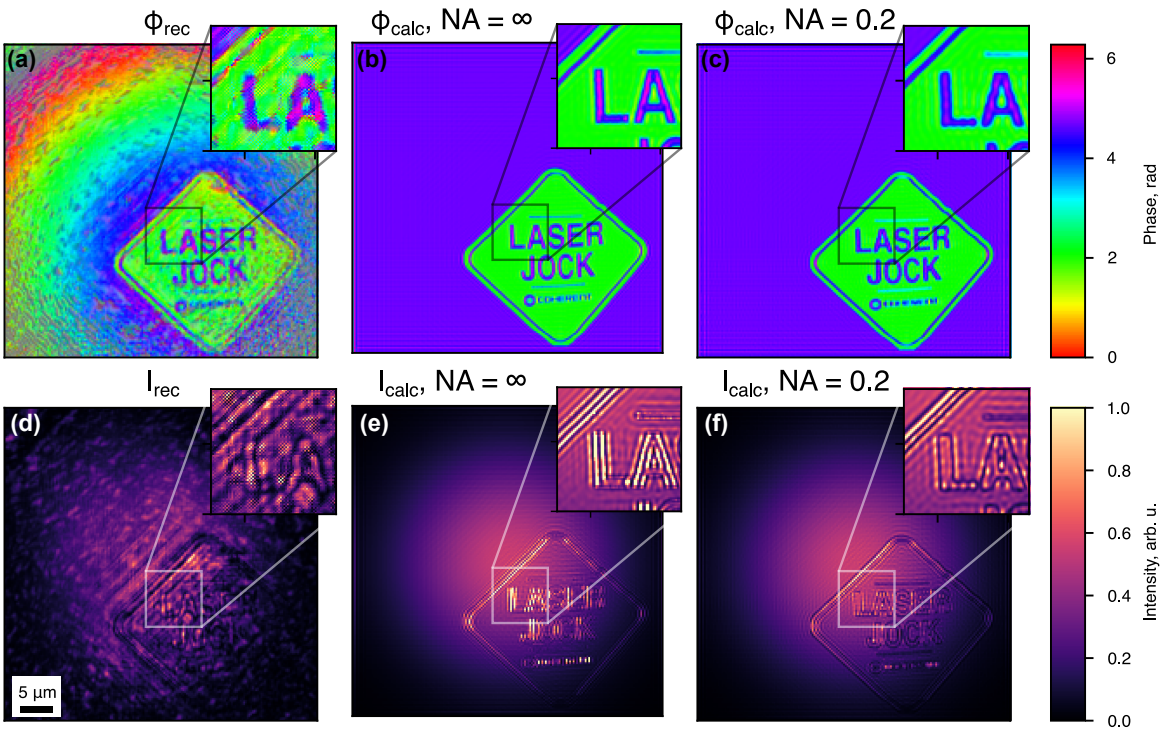

Fig. 4. (a) Reconstructed and (b), (c) calculated phase; and (d) reconstructed and (e), (f) calculated intensity profiles of the seventh harmonic field at the sample surface. (c), (f) Results of the calculations taking into account finite NA of the imaging. The insets shows magnified regions of the corresponding images. See text for the simulation details.

to only those within the acceptance cone of the detector results in smoother phase [Fig. 4(c)] and intensity [Fig. 4(f)] profiles. The remaining discrepancy can be attributed to the simplicity of our model that does not take into account generation and scattering of the XUV by the walls of the structure. In the unstructured regions of the sample, the reconstructed field also reveals additional spots not present in the calculations. These spots are possibly due to the inhomogeneity of the crystal, affecting the local HHG efficiency [35].

3. CONCLUSION

In conclusion, we demonstrate *in situ* XUV microscopy. Our approach allows us to reconstruct the phase and amplitude of XUV high-order harmonics emitted from aperiodic nanostructures etched on the surface of an MgO crystal. Our 3D modeling of the interaction reproduces the experimental amplitude and phase images, providing valuable guidance for the design of XUV metasurfaces. With shorter driving pulses [33], different crystals [36], and longer driving wavelengths [37], the harmonic cutoff can be increased to ∼40 eV [38], thus potentially improving the resolution. The increased high-harmonic cutoff and the ensuing large number of harmonics poses a challenge to lensless imaging. The increased bandwidth can be addressed with spectral filtering or potentially adapting previously developed broadband approaches [39,40]. Our *in situ* approach will pave the way for understanding and optimizing XUV high-harmonic metasurfaces and the eventual integration of XUV emitters on a chip. It also enables the direct imaging of strong-field processes in bulk and nanostructured solids, such as the effect of laser-induced damage, heating, and plasma on XUV high harmonics.

APPENDIX A

1. Optical Setup

The output from a Ti:Sapph regenerative amplifier (Coherent Legend, central wavelength 800 nm, pulse duration 45 fs FWHM, as measured with a TiPA autocorrelator, 1 kHz repetition rate) is focused with a 30 cm focal length plano–concave BK7 lens, to a peak field intensity of 4 TW/cm^2.

The imaging MCP detector is mounted on a translation stage, and can be moved out of the beam path, revealing an XUV spectrometer behind. The spectrum acquired with this spectrometer is plotted in Fig. 1(b), and is dominated by the seventh harmonic alone. Lower harmonics are below the sensitivity cutoff of the MCP spectrometer, while the higher ones are beyond the energy cutoff of the HHG. A similar conclusion can be drawn by looking directly at the diffraction image from a grating structure (Fig. 6), where a weak grid of diffraction orders with a larger spatial period, attributed to the fifth harmonic, can be observed in addition to the main one, attributed to the seventh harmonic.

Several main factors are taken into account when selecting the XUV mask. It should be completely opaque to the XUV, to simplify the theoretical treatment of the mask effect in the reconstruction, able to withstand intense laser fields, and be sufficiently thin to avoid scattering and absorption of the XUV from its side walls. A thin glass membrane satisfies all these criteria. We estimate the required thickness in our experiment to be $\lesssim 1$ μm. To produce such membrane, we heat a sealed glass tube and blow it into a sphere of a few tens of centimeters in diameter. We then shatter it into small submillimeter pieces, out of which a suitable one is selected under an optical microscope. The selected shard has a sharp apex and straight sides. While many other shapes also result

in reliable reconstruction of the field in numerical simulations, a triangular shape of the shard is chosen, since it is the easiest to produce with our approach. Additionally, it is simple to describe in the reconstruction algorithm, since it is fully parameterized by only two values: the angles between its sides and the vertical. These two angles were determined from a far-field diffraction image of the XUV, generated on the unstructured portion of the crystal, and confirmed with an optical microscope.

Far-field resolution determines the coordinate span in the plane of the mask. The technique requires the near field to be completely contained within this span for the relation between near and far fields to be unambiguous. This sets the upper bound for the distance between the sample and the mask: $L \lesssim D_x/(2\mathrm{NA}) \sim 325\ \mu\mathrm{m}$, where D_x is the coordinate span. If this distance is too large, the diffracted photon can miss the coordinate span in the plane of the mask, but still get detected on the MCP detector. Our chosen distance, $L = 247\ \mu\mathrm{m}$, satisfies this constraint.

The mask position is scanned in the (x, y) plane with high-resolution nanopositioners (Micronix). Its coordinates are selected from the set $(x, y) \in (A \times A) \cup (B \times B)$, where $A = \{-30, -15, \ldots 30\}\ \mu\mathrm{m}$, and $B = \{-20, -20/3, 20/3, 20\}\ \mu\mathrm{m}$. While this set resulted in a decent reconstruction, other possible mask movement patterns are yet to be explored.

2. Image Acquisition

Due to the sensitivity of the CDI reconstruction to the noise and its requirement of a high dynamic range, we develop a hit detection-based approach to the diffraction image acquisition. We employ a fast, 500 fps frame rate camera to capture a diffraction image from every second laser shot. With every shot containing only a few ($\lesssim 10$) detected photon hit events [Fig. 5(a)], there is a very little probability of their overlap, and every spike can be attributed to a single photon. Using a fast acquisition library, we threshold the image, and find the coordinates of the centers of individual hits with a marching squares algorithm, discarding the raw image afterwards [Fig. 5(b)]. These coordinates are then binned in a 512×512 2D histogram, and added to the histograms acquired from previous laser shots [Figs. 5(c) and 5(d)]. This approach allows us to collect very high-dynamic-range ($> 10^4$) images with almost no background noise. Comparing the off-axis event counts when illuminating the structured (1.6 events/laser shot) and unstructured (0.04 events/laser shot, coming mostly from the scattering from the surface corrugation) regions of the crystal, we can conclude that the intensity of the diffracted signal can be decreased by a factor of 40, before the signal-to-noise ratio (SNR) reaches unity, therefore making the phase reconstruction impossible. Consider the field amplitude with a small phase step $\Delta\varphi$: $E(x) = E_0 e^{ix\Delta\varphi H(x)}$, where $H(x)$ is the Heaviside function. Keeping only up to linear terms in the Taylor expansion in $\Delta\varphi$ and taking a Fourier transform, we can get the far-field intensity distribution $I(k_x) = |\mathcal{F}\{E_0(1 + ix\Delta\varphi H(x))\}|^2$. Here, only the second term contributes to the off-axis diffraction, $I(k_x \neq 0) = \Delta\varphi^2 E_0^2 |\mathcal{F}\{x H(x)\}|^2$, yielding a quadratic dependence on the phase step. This suggests that the phase contrast of our structures can be decreased $\sqrt{40} \approx 6$ times before SNR prohibits the measurement.

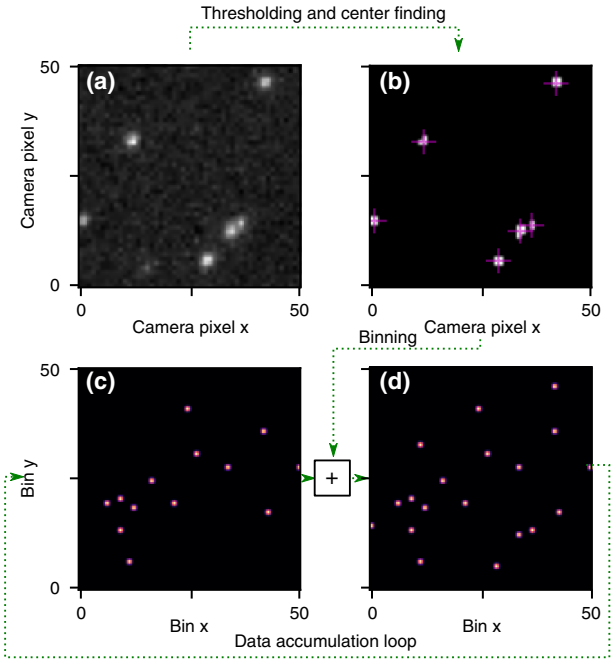

Fig. 5. Low-noise image acquisition. (a) Raw image from the camera, with clearly visible XUV photons hits. A small 50 px × 50 px region of the whole 512 px × 512 px detector is shown. (b) Thresholded image. Using a marching squares algorithm, we determine the centroids of each isolated hit (magenta crosses). (c) The centroids are binned in a 2D coordinate grid and added to the histogram, acquired in previous camera shots, to produce (d), an updated histogram.

3. Imaging Calibration

The images acquired this way are in the detector coordinates $(x_{\mathrm{MCP}}, y_{\mathrm{MCP}})$, and have to be converted to the reciprocal space of the mask or sample plane coordinates $k_\perp = (k_x, k_y)$. We use the diffraction image from a known structure, a 4 μm pitch 2D diffraction grating, patterned on the same sample [Fig. 6(a)]. We identify the coordinates of the diffraction orders, marked by red crosses, and perform the fit to a diffraction grating equation to find the distance and relative orientation of the two planes. Using those, we perform rectilinear interpolation of the original images onto a regular grid of (k_x, k_y). An example of such interpolation applied to the 2D grating diffraction image is shown in Fig. 6(b), revealing a periodic 2D grid of diffraction orders, inherent to the grating.

4. Reconstruction Algorithm

The algorithm reconstructs the complex electric field $F[i_x, i_y]$ in the plane of the mask from the N_{im} measured amplitudes $A_{i_{\mathrm{im}}}[i_x, i_y]$, $i_{\mathrm{im}} \in \{0, \ldots N_{\mathrm{im}} - 1\}$, after application of binary masks $M_{i_{\mathrm{im}}}[i_x, i_y]$. The mask arrays were determined from the shape of the mask and the coordinates of the nanopositioners. The image size is $N_x \times N_y$. Additional parameter $\beta = 0.5$ was used to improve the convergence.

5. Field Calculations

To lift the heavy memory requirements in the short wavelength regime, we split the field calculations into two separate steps: laser propagation and XUV propagation.

The first step employs a finite difference time domain method (FDTD) in a commercial software (Lumerical). The

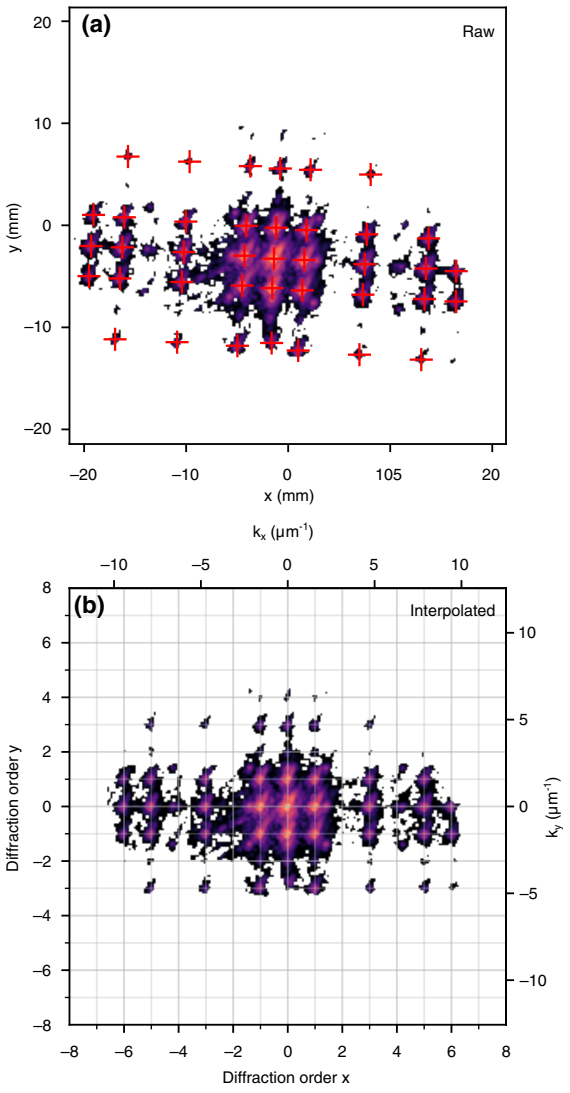

Fig. 6. Imaging calibration. (a) Raw diffraction image from a calibration 2D grating. Red crosses mark identified diffraction orders. Using the pixel coordinates of the diffraction orders allows us to precisely locate the MCP plane relative to the structure. (b) 2D grating diffraction image interpolated to a grid of regular $k_\perp$. Same interpolation is applied to every acquired diffraction image.

MgO crystal is modeled as a single dielectric/vacuum interface, with a height described with a two-valued function: $z = h(x, y) = -61\ \text{nm} \times I_{\text{logo}}(x, y)$, where $I_{\text{logo}}(x, y)$ is a binary image of the logo, used in the lithography:

$$I_{\text{logo}}(x, y) = \begin{cases} 0 & \text{in pristine regions,} \\ 1 & \text{in etched regions.} \end{cases}$$

The x-polarized laser pulse is then launched from the $z = -130$ nm plane in the positive z direction. We use a Gaussian beam profile with a waist radius of 60 μm, shifted by a few micrometers from the center of the logo to match the experimental conditions. The laser field is propagated through the structure, developing strong nanoscale modulations and near-field enhancements, and its complex amplitude $E^{\text{L}}(x, y, z)$ is recorded in the two planes, "top" and "bottom," $E^{\text{L}}_{\text{t}}(x, y) = E^{\text{L}}(x, y, z = -1\ \text{nm})$ and $E^{\text{L}}_{\text{b}} = E^{\text{L}}(x, y, z = -61\ \text{nm})$, and exported to be processed in a Python script in the second step of calculations. The planes are chosen to be slightly below the surface of the pristine (top) and etched (bottom) regions of the crystal.

$F = \text{random}(N_x, N_y)$
for i_{iter} **in** $0 \dots N_{\text{maxiter}} - 1$ **do**
  for i_{im} **in** $0 \dots N_{\text{im}} - 1$ **do**
    $E_{i_{\text{im}}} \Leftarrow \mathcal{F}^{-1}\{F\}$
    for i_x, i_y **in** $\{0 \dots N_x - 1\} \times \{0 \dots N_y - 1\}$ **do**
      $EM_{i_{\text{im}}}[i_x, i_y] \Leftarrow E_{i_{\text{im}}}[i_x, i_y] \times M_{i_{\text{im}}}[i_x, i_y]$
    end for
    $F_{i_{\text{im}}} \Leftarrow \mathcal{F}\{EM_{i_{\text{im}}}\}$
    $F_{i_{\text{im}}} \Leftarrow A_{i_{\text{im}}} \times F_{i_{\text{im}}}/|F_{i_{\text{im}}}|$
    $EM_{i_{\text{im}}} \Leftarrow \mathcal{F}^{-1}\{F_{i_{\text{im}}}\}$
    for i_x, i_y **in** $\{0 \dots N_x - 1\} \times \{0 \dots N_y - 1\}$ **do**
      if $M_{i_{\text{im}}}[i_x, i_y]$ **is** 1 **then**
        $E_{i_{\text{im}}}[i_x, i_y] \Leftarrow (1 - \beta) \times E_{i_{\text{im}}}[i_x, i_y] + \beta \times EM_{i_{\text{im}}}[i_x, i_y]$
      end if
    end for
    $F \Leftarrow \mathcal{F}\{E_{i_{\text{im}}}\}$
  end for
  $err \Leftarrow \sum_{i_{\text{im}}, i_x, i_y} ||F_{i_{\text{im}}}| - A_{i_{\text{im}}}|^2$
end while

To perform the XUV calculations, we first model the expected XUV field generated in the crystal as

$$E^{\text{XUV}}_{\text{t}}(x, y) = \left|E^{\text{L}}_{\text{t}}(x, y)\right|^{n_{\text{s}}} e^{7i \arg E^{\text{L}}_{\text{t}}(x,y)} (1 - I_{\text{logo}}(x, y)),$$

and

$$E^{\text{XUV}}_{\text{b}}(x, y) = \left|E^{\text{L}}_{\text{b}}(x, y)\right|^{n_{\text{s}}} e^{7i \arg E^{\text{L}}_{\text{b}}(x,y)} I_{\text{logo}}(x, y).$$

Here, $n_{\text{s}} = 7$ was an experimentally determined intensity scaling power of the seventh harmonic, and the factors containing $I_{\text{logo}}(x, y)$ reflect the fact that the harmonics are generated only near the dielectric/vacuum interface, due to the XUV absorption. We emphasize that while we do employ this simple model here to describe the observed field profiles, our reconstruction technique does not rely on any physical model of HHG, as it measures the XUV directly.

We then propagate $E^{\text{XUV}}_{\text{b}}(x, y)$ to the top plane $z = -1$ nm in 10 consecutive steps. On each step, the field is propagated by $\Delta z = 6$ nm using a plane-wave expansion, and multiplied by $I_{\text{logo}}(x, y)$, to model the XUV absorption in the walls of the structure. The total XUV field at the exit plane $E^{\text{XUV}}(x, y)$ is found as the sum of $E^{\text{XUV}}_{\text{t}}(x, y)$ and $E^{\text{XUV}}_{\text{b}}(x, y)$, propagated as described above.

Finally, to compare our calculated field with the experimental results, we expanded the $E^{\text{XUV}}(x, y)$ in a plane-wave base, keeping only the waves within our experimental NA = 0.2. The phase and intensity of the resulting calculated field are plotted in Figs. 4(c) and 4(f), respectively.

Funding. Joint Center for Extreme Photonics; Defense Threat Reduction Agency (HDTRA 1-19-1-0026); Air Force Office of Scientific Research (FA9550-16-1-0109); Natural Sciences and Engineering Research Council of Canada; W. M. Keck Foundation.

Acknowledgment. The authors thank David Crane and Ryan Kroeker for providing continuing technical support and Lora Ramunno for fruitful discussions. G. V., A. K., and P. B. C. acknowledge support from the Joint Center for Extreme Photonics. P. B. C. acknowledges funds from the U.S. Defence Threat Reduction and from the U.S. Air Force Office of Scientific Research.

P. B. acknowledges funding from the Natural Sciences and Engineering Research Council of Canada. D. A. R. acknowledges funding from the W. M. Keck foundation. A. K. conceived the experiment, performed the optical measurements, and analyzed the data, S. R. produced the MgO sample, A. N. maintained the laser system, D. V., D. A. R., P. B., and P. B. C. supervised the work. G. V. performed calculations and supervised the work.

Disclosures. The authors declare no conflicts of interest.

Data availability. Data underlying the results presented in this paper are not publicly available at this time but may be obtained from the authors upon reasonable request.

REFERENCES

1. A. Korobenko, S. Rashid, C. Heide, A. Y. Naumov, D. A. Reis, P. Berini, P. B. Corkum, and G. Vampa, "Generation of structured coherent extreme ultraviolet beams from an MgO crystal," Opt. Express **29**, 24161–24168 (2021).
2. S. D. C. Roscam Abbing, R. Kolkowski, Z.-Y. Zhang, F. Campi, L. Lötgering, A. F. Koenderink, and P. M. Kraus, "Extreme-ultraviolet shaping and imaging by high-harmonic generation from nanostructured silica," Phys. Rev. Lett. **128**, 223902 (2022).
3. S. Han, H. Kim, Y. W. Kim, Y.-J. Kim, S. Kim, I.-Y. Park, and S.-W. Kim, "High-harmonic generation by field enhanced femtosecond pulses in metal-sapphire nanostructure," Nat. Commun. **7**, 13105 (2016).
4. M. Sivis, M. Taucer, G. Vampa, K. Johnston, A. Staudte, A. Y. Naumov, D. M. Villeneuve, C. Ropers, and P. B. Corkum, "Tailored semiconductors for high-harmonic optoelectronics," Science **357**, 303–306 (2017).
5. G. Vampa, B. G. Ghamsari, S. Siadat Mousavi, T. J. Hammond, A. Olivieri, E. Lisicka-Skrek, A. Y. Naumov, D. M. Villeneuve, A. Staudte, P. Berini, and P. B. Corkum, "Plasmon-enhanced high-harmonic generation from silicon," Nat. Phys. **13**, 659–662 (2017).
6. H. Liu, C. Guo, G. Vampa, J. L. Zhang, T. Sarmiento, M. Xiao, P. H. Bucksbaum, J. Vučković, S. Fan, and D. A. Reis, "Enhanced high-harmonic generation from an all-dielectric metasurface," Nat. Phys. **14**, 1006–1010 (2018).
7. M. R. Shcherbakov, H. Zhang, M. Tripepi, G. Sartorello, N. Talisa, A. AlShafey, Z. Fan, J. Twardowski, L. A. Krivitsky, A. I. Kuznetsov, E. Chowdhury, and G. Shvets, "Generation of even and odd high harmonics in resonant metasurfaces using single and multiple ultra-intense laser pulses," Nat. Commun. **12**, 4185 (2021).
8. G. Zograf, K. Koshelev, A. Zalogina, V. Korolev, R. Hollinger, D.-Y. Choi, M. Zuerch, C. Spielmann, B. Luther-Davies, D. Kartashov, S. V. Makarov, S. S. Kruk, and Y. Kivshar, "High-harmonic generation from resonant dielectric metasurfaces empowered by bound states in the continuum," ACS Photon. **9**, 567–574 (2022).
9. H. Liu, G. Vampa, J. L. Zhang, Y. Shi, S. Buddhiraju, S. Fan, J. Vuckovic, P. H. Bucksbaum, and D. A. Reis, "Beating absorption in solid-state high harmonics," Commun. Phys. **3**, 192 (2020).
10. D. Gauthier, S. Kaassamani, D. Franz, R. Nicolas, J.-T. Gomes, L. Lavoute, D. Gaponov, S. Février, G. Jargot, M. Hanna, W. Boutu, and H. Merdji, "Orbital angular momentum from semiconductor high-order harmonics," Opt. Lett. **44**, 546–549 (2019).
11. E. N. Leith and J. Upatnieks, "Reconstructed wavefronts and communication theory*," J. Opt. Soc. Am. **52**, 1123–1130 (1962).
12. S. Eisebitt, J. Lüning, W. F. Schlotter, M. Lörgen, O. Hellwig, W. Eberhardt, and J. Stöhr, "Lensless imaging of magnetic nanostructures by x-ray spectro-holography," Nature **432**, 885–888 (2004).
13. M. Guizar-Sicairos and J. R. Fienup, "Holography with extended reference by autocorrelation linear differential operation," Opt. Express **15**, 17592–17612 (2007).
14. D. Gauthier, M. Guizar-Sicairos, X. Ge, W. Boutu, B. Carré, J. R. Fienup, and H. Merdji, "Single-shot femtosecond x-ray holography using extended references," Phys. Rev. Lett. **105**, 093901 (2010).
15. Y. Meng, C. Zhang, C. Marceau, A. Y. Naumov, P. B. Corkum, and D. M. Villeneuve, "Octave-spanning hyperspectral coherent diffractive imaging in the extreme ultraviolet range," Opt. Express **23**, 28960–28969 (2015).
16. J. R. Fienup, "Reconstruction of an object from the modulus of its Fourier transform," Opt. Lett. **3**, 27–29 (1978).
17. J. Miao, P. Charalambous, J. Kirz, and D. Sayre, "Extending the methodology of x-ray crystallography to allow imaging of micrometre-sized non-crystalline specimens," Nature **400**, 342–344 (1999).
18. Y. Shechtman, Y. C. Eldar, O. Cohen, H. N. Chapman, J. Miao, and M. Segev, "Phase retrieval with application to optical imaging: a contemporary overview," IEEE Signal Process. Mag. **32**(3), 87–109 (2015).
19. D. E. Adams, B. Zhang, M. D. Seaberg, D. F. Gardner, E. R. Shanblatt, M. M. Murnane, and H. C. Kapteyn, "Tabletop nanometer extreme ultraviolet imaging in an extended reflection geometry," in *Frontiers in Optics*, OSA, Washington, D.C., USA, 2014), Vol. **1**, paper LW1H.4.
20. J. Bertolotti, E. G. van Putten, C. Blum, A. Lagendijk, W. L. Vos, and A. P. Mosk, "Non-invasive imaging through opaque scattering layers," Nature **491**, 232–234 (2012).
21. R. L. Sandberg, A. Paul, D. A. Raymondson, S. Hädrich, D. M. Gaudiosi, J. Holtsnider, R. I. Tobey, O. Cohen, M. M. Murnane, H. C. Kapteyn, C. Song, J. Miao, Y. Liu, and F. Salmassi, "Lensless diffractive imaging using tabletop coherent high-harmonic soft-x-ray beams," Phys. Rev. Lett. **99**, 098103 (2007).
22. A. Ravasio, D. Gauthier, F. R. N. C. Maia, *et al.*, "Single-shot diffractive imaging with a table-top femtosecond soft x-ray laser-harmonics source," Phys. Rev. Lett. **103**, 028104 (2009).
23. M. D. Seaberg, D. E. Adams, E. L. Townsend, D. A. Raymondson, W. F. Schlotter, Y. Liu, C. S. Menoni, L. Rong, C.-C. Chen, J. Miao, H. C. Kapteyn, and M. M. Murnane, "Ultrahigh 22 nm resolution coherent diffractive imaging using a desktop 13 nm high harmonic source," Opt. Express **19**, 22470–22479 (2011).
24. H. N. Chapman, A. Barty, M. J. Bogan, *et al.*, "Femtosecond diffractive imaging with a soft-x-ray free-electron laser," Nat. Phys. **2**, 839–843 (2006).
25. J. Miao, T. Ishikawa, B. Johnson, E. H. Anderson, B. Lai, and K. O. Hodgson, "High resolution 3D x-ray diffraction microscopy," Phys. Rev. Lett. **89**, 088303 (2002).
26. I. K. Robinson, I. A. Vartanyants, G. J. Williams, M. A. Pfeifer, and J. A. Pitney, "Reconstruction of the shapes of gold nanocrystals using coherent x-ray diffraction," Phys. Rev. Lett. **87**, 195505 (2001).
27. S. Zayko, M. Sivis, S. Schäfer, and C. Ropers, "Polarization contrast of nanoscale waveguides in high harmonic imaging," Optica **3**, 239–242 (2016).
28. E. R. Shanblatt, C. L. Porter, D. F. Gardner, G. F. Mancini, R. M. Karl, M. D. Tanksalvala, C. S. Bevis, V. H. Vartanian, H. C. Kapteyn, D. E. Adams, and M. M. Murnane, "Quantitative chemically specific coherent diffractive imaging of reactions at buried interfaces with few nanometer precision," Nano Lett. **16**, 5444–5450 (2016).
29. O. Kfir, S. Zayko, C. Nolte, M. Sivis, M. Möller, B. Hebler, S. S. P. K. Arekapudi, D. Steil, S. Schäfer, M. Albrecht, O. Cohen, S. Mathias, and C. Ropers, "Nanoscale magnetic imaging using circularly polarized high-harmonic radiation," Sci. Adv. **3**, 1–6 (2017).
30. M. Odstrcil, P. Baksh, C. Gawith, R. Vrcelj, J. G. Frey, and W. S. Brocklesby, "Nonlinear ptychographic coherent diffractive imaging," Opt. Express **24**, 20245–20252 (2016).
31. S. Fröhlich, X. Liu, A. Hamdou, A. Meunier, M. Hussain, M. Carole, S. Kaassamani, M. Froidevaux, L. Lavoute, D. Gaponov, N. Ducros, S. Février, P. Zeitoun, M. Kovacev, M. Fajardo, W. Boutu, D. Gauthier, and H. Merdji, "Self-probed ptychography from semiconductor high-harmonic generation," Opt. Lett. **47**, 4865–4868 (2022).
32. Y. S. You, M. Wu, Y. Yin, A. Chew, X. Ren, S. Gholam-Mirzaei, D. A. Browne, M. Chini, Z. Chang, K. J. Schafer, M. B. Gaarde, and S. Ghimire, "Laser waveform control of extreme ultraviolet high harmonics from solids," Opt. Lett. **42**, 1816–1819 (2017).
33. A. Korobenko, T. J. Hammond, C. Zhang, A. Y. Naumov, D. M. Villeneuve, and P. B. Corkum, "High-harmonic generation in solids driven by counter-propagating pulses," Opt. Express **27**, 32630–32637 (2019).
34. J. Lu, E. F. Cunningham, Y. S. You, D. A. Reis, and S. Ghimire, "Interferometry of dipole phase in high harmonics from solids," Nat. Photonics **13**, 96–100 (2019).
35. V. E. Nefedova, S. Fröhlich, F. Navarrete, N. Tancogne-Dejean, D. Franz, A. Hamdou, S. Kaassamani, D. Gauthier, R. Nicolas, G. Jargot, M. Hanna, P. Georges, M. F. Ciappina, U. Thumm, W. Boutu, and H. Merdji, "Enhanced extreme ultraviolet high-harmonic generation from chromium-doped magnesium oxide," Appl. Phys. Lett. **118**, 201103 (2021).

36. T. T. Luu, M. Garg, S. Y. Kruchinin, A. Moulet, M. T. Hassan, and E. Goulielmakis, "Extreme ultraviolet high-harmonic spectroscopy of solids," Nature **521**, 498–502 (2015).
37. Y. S. You, D. A. Reis, and S. Ghimire, "Anisotropic high-harmonic generation in bulk crystals," Nat. Phys. **13**, 345–349 (2017).
38. S. Ghimire and D. A. Reis, "High-harmonic generation from solids," Nat. Phys. **15**, 10–16 (2019).
39. B. Abbey, L. W. Whitehead, H. M. Quiney, D. J. Vine, G. A. Cadenazzi, C. A. Henderson, K. A. Nugent, E. Balaur, C. T. Putkunz, A. G. Peele, G. J. Williams, and I. McNulty, "Lensless imaging using broadband x-ray sources," Nat. Photonics **5**, 420–424 (2011).
40. A. Rana, J. Zhang, M. Pham, A. Yuan, Y. H. Lo, H. Jiang, S. J. Osher, and J. Miao, "Potential of attosecond coherent diffractive imaging," Phys. Rev. Lett. **125**, 086101 (2020).